Nanoscience and Nanotechnology Letters
Vol. 10, 1–6, 2018

Analysis of Laser Sintering of Zirconia to Magnesium Alloy by Laser-Induced Plasma Spectroscopy

Sangwoo Yoon, Ji-Hun Kim, Woo-Tae Park, and Joohan Kim*

Department of Mechanical Engineering, Seoul National University of Science and Technology, Seoul, 01811, Korea

The effects of laser energy on the sintering of zirconia (ZrO_2) on a magnesium (Mg) alloy were studied. The sintered surface was resistant to corrosion by Na_2SO_4 solution. The surface micro-nano structure and cross-sectional micro-nano structure of the sintered layer were observed by optical microscopy and scanning electron microscopy (SEM). Incomplete sintering was observed at low volumetric laser energy levels (0.38–0.51 MJ/cm^3). Defects in the sintered and diffusion layers, and a thinner diffusion layer, were observed at a high volumetric laser energy levels (1.27–1.70 MJ/cm^3). At an intermediate volumetric laser energy level (0.64–0.76 MJ/cm^3), the sintered layer quality was high and the ZrO_2 sintered layer and diffusion layer were balanced. Elemental analysis of the sintered ZrO_2 layer and the diffusion layer was performed using laser-induced breakdown spectroscopy (LIBS). The thickness of the diffusion layer in the sintered region was measured and the diffusion of elemental Zr was analyzed. The diffusion coefficient of ZrO_2 (0.94–41.67 μm^2/s) was also determined by analyzing the concentration of Zr in the diffusion layer.

Keywords: Corrosion Surface, Laser Sintering, Laser-Induced Breakdown Spectroscopy, Mg Alloy, Surface Treatment, Zirconia.

1. INTRODUCTION

Magnesium (Mg) alloys are lightweight, high-strength metals that are used in the automotive, aerospace, electronics, and biotechnology industries.[1] However, their vulnerability to corrosion limits applications of these alloys.[2–4] Hence, surface treatment of Mg alloys to offset these disadvantages is of great importance. Sintering of ceramic coatings on metal materials is a widely used type of surface treatment.[5,6] Surface coating with zirconia (ZrO_2) is attractive because it can reduce oxidation, prevent corrosion, thermally insulate, and enhance the surface strength of materials.[7,8] Specifically, Mg–ZrO_2 sintering, which sinters coatings of ZrO_2 on Mg alloys, prevents corrosion of the Mg substrate and increases surface strength.

The reaction at the interface between two materials is very important during the sintering of ceramic-coated metal surfaces. This reaction has decisive influence on the coating bonding properties.[9,10] For example, interfacial reactions of metal–ceramic compounds strongly influence the mechanical and functional properties of ceramic composites.[11–14]

Sintering methods for metals include reaction sintering,[15] pressure sintering,[16] spark plasma sintering,[17] and sol–gel coating.[18] Reaction sintering is performed by chemical reaction in a closed vessel in the presence of a gas. Pressure sintering forms a powder at high pressure. Discharge plasma sintering applies pressure and voltage to a powder. Among the methods used to sinter ceramic coatings on a metal surface, laser sintering is particularly advantageous because it can be applied to various materials: it constrains the laser energy locally and thereby minimizes heating of the substrate. Laser machining selectively liquefies powder on the surface of a specimen very rapidly. In this way, the surface properties of a specific region of precision-machined parts can be readily modified. Also, the influence of the heat-affected zone (HAZ) generated during the bonding process can be minimized through precise laser energy control. Laser sintering does not require pressure, gas, or a confined space, and demands less technical skill to implement. Sintering can also be accomplished in a relatively short time.[19–22]

X-ray diffraction (XRD), X-ray photoelectron spectroscopy (XPS), scanning electron microscopy (SEM), and energy dispersive spectroscopy (EDS) have been used to characterize ZrO_2 coatings on Mg alloys.[15,23,24] Preprocessing and postprocessing can greatly affect measurements derived from these techniques. Although the methods are time-consuming, the same specimen can be used to obtain additional data in some cases. Recently, techniques for measuring physical properties using lasers have been developed.

*Author to whom correspondence should be addressed.

Laser-induced breakdown spectroscopy (LIBS) analyzes the plasma signal generated from the surface by the laser. The focused laser beam is irradiated onto the surface of the sample, which generates a plasma. This plasma atomizes and ionizes elements that are present on the surface; the emission spectrum is characteristic of the elements and their energy states. LIBS uses spectral analysis to provide qualitative and quantitative information concerning the test material. Although LIBS vaporizes the specimen and ionizes it into a plasma, the amount of material is very small and so it can be considered a non-destructive test method. The small amount of material, short analysis time, and minimal pre- and post-treatment makes it possible to monitor elemental composition in real time. Additionally, the laser can generate microholes through the surface of the specimen so that the interior of the material can be analyzed.[25]

In this study, ZrO_2 powder was sintered on the surface of an Mg alloy using a laser beam. The thickness of the Mg–ZrO_2 compound layer was controlled by adjusting the laser power. The corrosion resistance of the surfaces of samples having different ZrO_2 coating thicknesses was measured to explore the effect of the coating. LIBS was used to analyze the Mg–ZrO_2 compound layer. The nanoscale diffusion characteristics was verified and the diffusion coefficient of the material migrating from the coating to the substrate was estimated.

2. EXPERIMENTAL DETAILS

The composition of the Mg alloy (AZ91D) used in the experiments is given in Table I. The surface of the Mg alloy was coated with ZrO_2 powder and sintered using a laser. The ZrO_2 powder was mixed with a small amount of Na_2SiO_3 solution to increase the initial adhesion of the powder to the Mg surface before sintering. After laser sintering, the Mg surface was covered with 40–250 μm-sized ZrO_2 granules. The thickness of the sintered layer was ca. 90–250 μm and the sintered area had dimensions 4×4 mm^2.

The laser used for laser sintering was a continuous-wave (CW) fiber laser with a wavelength of 1,070 nm (YLR-50-SM-AC; IPG); the experimental set-up is shown in Figure 1. The scanning path of the laser beam was controlled by a 100-mm focal length galvanometer, and the specimen was transported using a micro-motion stage. The laser process conditions are given in Table II. The laser scanning pattern was linear and overlapping was set at 10%. The surface and cross-sectional morphologies of laser-sintered Mg specimens were examined by optical microscopy (BX51M; Olympus) and scanning electron microscopy (SU8010; Hitachi). The composition of the coating layer after sintering was analyzed by LIBS and SEM up to nanoscale. The diffusion coefficient of the sintered layer was derived from the LIBS results. To evaluate

Table I. Chemical composition of the AZ91D alloy (wt%).

Mg	Al	Zn	Mn	Si	Fe	Cu	Ni
Bal.	9.1	0.74	0.12	<0.2	0.005	0.015	0.001

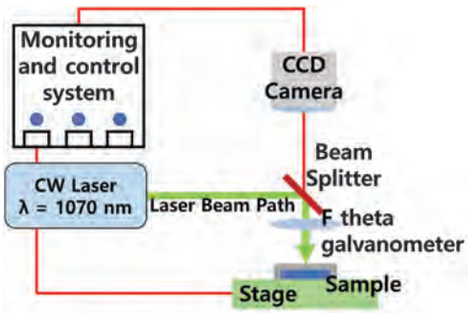

Fig. 1. Schematic diagram of the experimental set-up.

Table II. Laser parameters for sintering.

Volumetric laser energy density (MJ/cm^3)	Scan speed (mm/s)	Wave length (nm)	Scanning area (mm^2)	Laser spot size (μm)	Process time (s)
0.38–1.70	15–20	1,070	16	50–300	15

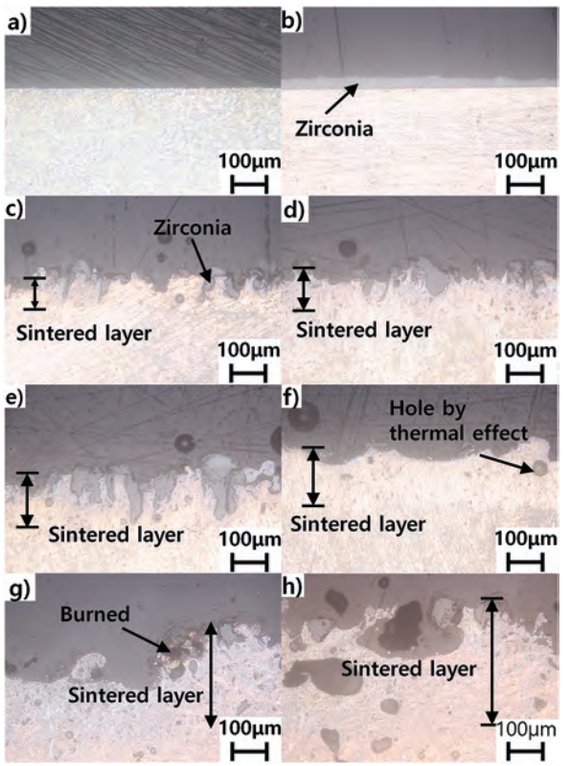

Fig. 2. Optical microscopy image of cross-sectional micro-nano structures of the sintered layer as a function of volumetric laser energy density. (a) No treatment, (b) 0.38 (MJ/cm^3), (c) 0.51 (MJ/cm^3), (d) 0.64 (MJ/cm^3), (e) 0.76 (MJ/cm^3), (f) 0.89 (MJ/cm^3), (g) 1.27 (MJ/cm^3), and (h) 1.70 (MJ/cm^3).

the surface corrosion resistance of the Mg alloy as a function of the laser process parameters, the specimens before and after sintering were exposed to 10% Na_2SO_4 solution for 50 h to initiate corrosion. The distributions of oxygen in the samples were measured with LIBS to evaluate the corrosion resistance. It is necessary to quantify the laser energy used to generate the plasma for consistent sintering analysis. For this purpose, volumetric laser energy density was calculated from the laser power density and the laser beam transport speed. The scanning speed was 15–20 mm/s.

The LIBS (RT100; Applied Spectra) used an Nd:YAG pulse laser operating at a wavelength of 1,070 nm. The laser provided an energy of 45 mJ per pulse and a pulse width of up to 5 ns. Spectral data collection was done at room temperature and atmospheric pressure. The LIBS laser was irradiated onto the material surface through a focusing lens; the spot size of the ablation for plasma generation was ca. 300 μm. The plasma spectral line was analyzed using a five-channel charge-coupled device (CCD) camera. The spectrometer detected a plasma wavelength ranging from 180 to 900 nm and set the gate delay time of the detector to 1 μs. The detected elemental spectral lines were analyzed using a data analysis program (Aurora; Applied Spectra).

3. RESULTS AND DISCUSSION

3.1. Micro-Nano Structure of the Sintered Layer

The surface of the sintered layer consisted of micron-sized clusters of ZrO_2 particles. Figure 2 shows the cross-sectional morphologies as a function of the laser parameters. The volumetric laser energy density was defined as laser power density per scanning velocity. Sintering of the ZrO_2 coating was incomplete at the low volumetric laser energy density of 0.38 MJ/cm^3. As a result, Mg surface traces of ZrO_2 were detected. When the volumetric laser energy density was increased to 0.51 MJ/cm^3, a uniform ZrO_2 surface was obtained with a thickness of 90 μm. A sintered surface layer was present even when the volumetric laser energy density reached 0.89 MJ/cm^3. However, a micro porous region formed in the specimen during the sintering process due to melting and solidification. At a higher volumetric laser energy density (1.27 MJ/cm^3), the size of the sintered particles was greater than 100 μm. Multiple cavities and extended micro porous regions were observed in the cross-section, and sintered particles were finely crushed or agglomerated. Figure 3 shows the surface morphologies and the nanoscale structures of a boundary between diffusion area Mg and zirconia. The interface of two materials shows a behavior of magnesium and zirconia. To observe the corrosion resistance of the sintered

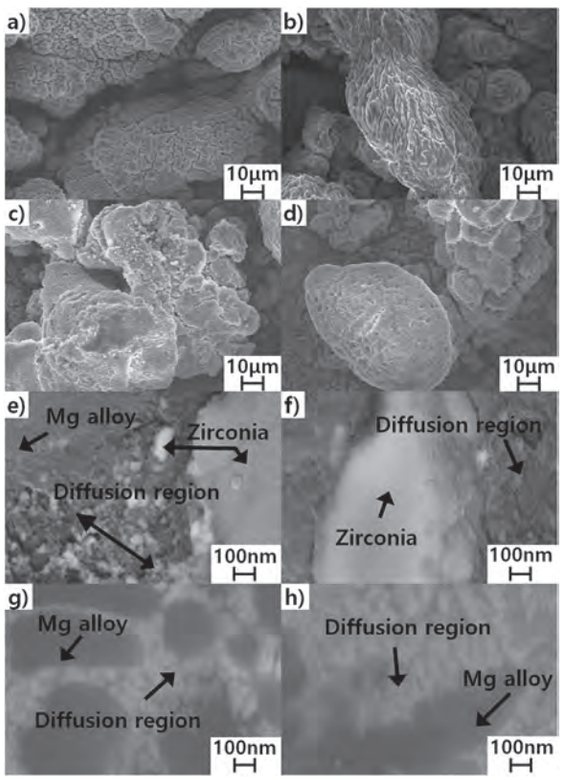

Fig. 3. Scanning electron microscopy (SEM) image of surface (a–d) and cross-sectional (e–h) micro-nano structures of the sintered layer as a function of laser energy density. (a, b, e, f) 0.51 (MJ/cm^3), (c, g) 0.64 (MJ/cm^3), and (d, h) 0.76 (MJ/cm^3).

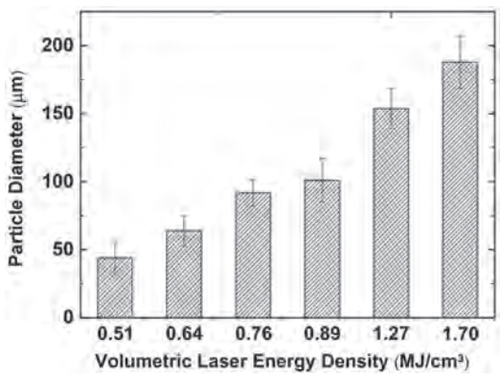

Fig. 4. Particle size as a function of laser energy density.

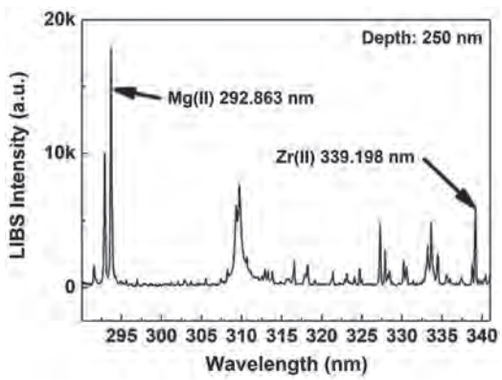

Fig. 5. Laser-induced breakdown spectroscopy (LIBS) spectral lines for magnesium (Mg) and zirconia (Zr) at 250 nm depth.

layer, the presence of oxide in the sintered layer was confirmed by treatment with the aqueous Na_2SO_4 solution. The mean sintered particle size increased with increasing laser energy density (Fig. 4). Increased sintered particle size in turn increased the surface roughness and could lead to the formation of micro cracks and increased brittleness in harsh external environments. The size of the particles was 40–240 μm. The most uniform grain formation was observed with a volumetric laser energy density of 0.64–0.76 (MJ/cm^3). The sintered layer was 100–300 μm deep and depended on the laser energy density.

3.2. Analysis of the Interfacial Layer

Analysis of the sintered interfacial layer was carried out by LIBS. Spectral lines at 292.863 and 339.198 nm corresponded to Mg (II) and Zr (II), respectively (Fig. 5).

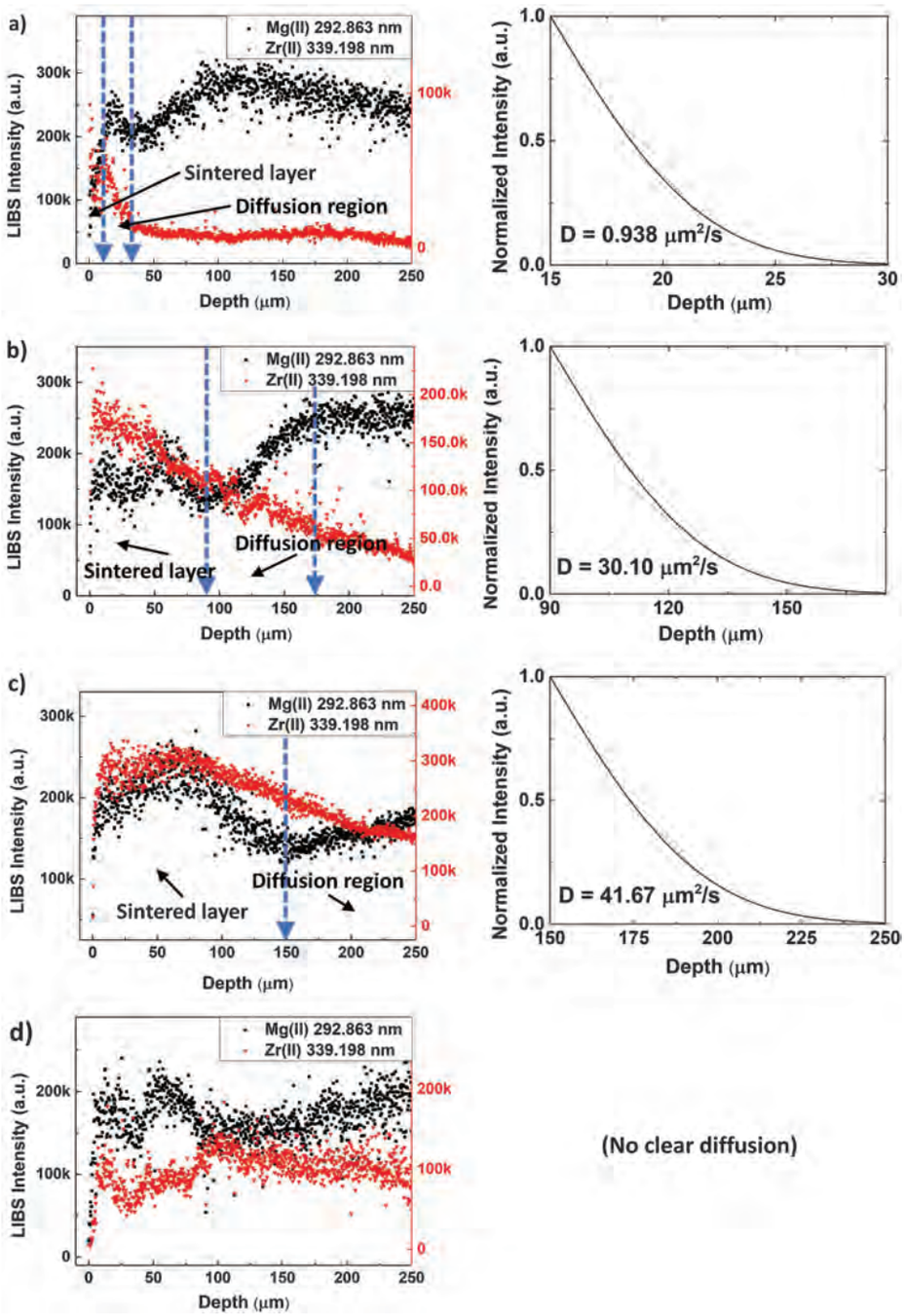

Fig. 6. LIBS spectral line intensity and diffusion as a function of depth. (a) 0.38 (MJ/cm^3), (b) 0.51 (MJ/cm^3), (c) 0.64 (MJ/cm^3), and (d) 1.70 (MJ/cm^3).

The specimens were irradiated by the lasers at an energy of 63.7 J/cm^2 per pulse, and spectral line data were collected from the surface to ca. 250 μm deep (Fig. 6). Each laser pulse generated a microhole ca. 250 nm deep; LIBS data were accumulated for each of 1,000 pulses to a depth of 250 μm, and minimum depth measured by LIBS is 250 nm. The sintered and diffusion layers were characterized by the relative intensity of the observed spectral line peaks for Mg and Zr. The sintered layer displayed peaks only for Zr. In the diffusion layer, Zr had diffused into Mg to form a compound layer; hence, signals for both Mg and Zr were observed, with those for Mg being more intense. The diffusion layer in which ZrO_2 diffused into the base material and the sintered region both thickened as the laser energy increased. The sintered region was thickened from 30 to 250 μm as the laser energy increased from 0.38 to 1.70 MJ/cm^3. The sintered and diffusion regions were also analyzed at each laser energy level. At low energy levels, the diffusion region was thicker than the region where only sintering occurred. The diffusion region decreased in thickness with increasing laser energy. Notably, diffusion into the Mg base material had stabilized when the energy per laser volume was 0.64 and 0.76 MJ/cm^3.

The diffusion behavior of ZrO_2 was characterized by estimating the diffusion coefficient through modeling the change in concentration of Zr obtained through LIBS. The change in elemental concentration can be expressed as a function of the diffusion coefficient according to Fick's law,

$$J = -D\frac{dC}{dx}$$

where J is the diffusion flow, D is the diffusion coefficient, and x is the depth. The diffusion flow is proportional to the concentration gradient of the material, where the diffusion coefficient is a constant. The one-dimensional governing equation of this diffusion flow is as follows:

$$\frac{\partial C(x,t)}{\partial t} = D\frac{\partial^2 C}{\partial x^2}$$

The diffusion coefficient D can be derived from the diffusion flow and concentration gradient. The solution of the governing equations for the diffusion of matter in the transient state of the governing equations is as follows:

$$\frac{C(x,t) - C_0}{C_1 - C_0} = 1 - erf\left(\frac{x}{2\sqrt{Dt}}\right)$$

where C_0 is the initial concentration, C_l is the final convergence concentration, and $C(x,t)$ is the concentration at time t at depth x. Experimentally obtained concentration changes were curve-fitted to the error function using this relationship, from which the diffusion coefficient of the sintered material was derived (Fig. 6). The value of the diffusion coefficient increased with increasing laser energy, reaching a maximum at 0.64 MJ/cm^3. Clearly, it is shown that diffusion is a function of laser energy.

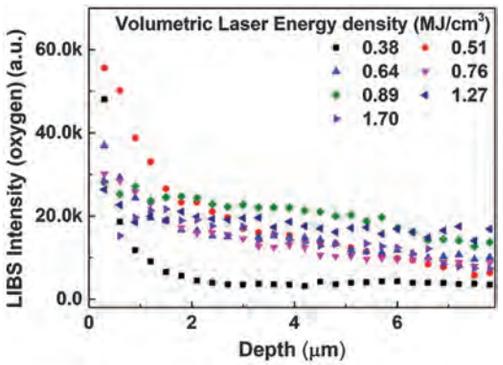

Fig. 7. Intensity of the oxygen spectral line as a function of depth from the corrosion surface for different volumetric laser energy densities.

The corrosion resistance of sintered surface-treated specimens was analyzed by LIBS; the presence of oxidized compounds indicated corrosion. The sintered specimens were exposed to 1 M Na_2SO_4 solution for 50 h and the micro-nano structures of the corroded specimens were measured by LIBS. Figure 7 shows the oxygen intensity data as a function of depth from the surface. In the case of specimens sintered with a laser energy of 0.38 MJ/cm^3, the solidified layer of sintered ZrO_2 protected the Mg substrate from the etchant, and thus the oxygen concentration along the layer was low. The oxygen concentration at the surface was highest when the laser energy was 0.51 MJ/cm^3, but this concentration decreased sharply with increasing distance from the surface. The results indicate that the corrosion resistance of the surface-sintered region increased with increasing laser energy.

4. CONCLUSION

The effect of laser energy level on the sintering of a ZrO_2 coating was studied. A fiber laser was used to sinter ZrO_2 particles on an Mg alloy surface. The volumetric laser energy density used in the process ranged from 0.38 to 1.70 MJ/cm^3. Sintering progress for each laser energy level was determined by examination of the surface and cross-sectional structures up to nanoscale. At low laser energy, a localized, non-homogeneous sintered layer was observed. Defects in the sintering solidification layer and the diffusion layer were noted at high laser energies; the optimal volumetric laser energy density for sintering was 0.64–0.76 MJ/cm^3. The concentration of ZrO_2 in the sintered layer was analyzed using LIBS, from which the diffusion coefficient was calculated. Such quantification of the diffusion coefficient enabled characterization of the diffusion layer under different sintering conditions. The oxygen concentration on the sintering side, as measured by LIBS, was used as an indicator of corrosion resistance; this was determined as a function of the laser energy.

Acknowledgments: This study was supported by the Research Program funded by the SeoulTech (Seoul National University of Science and Technology).

References and Notes

1. J. J. Zhuang, Y. Q. Guo, N. Xiang, Y. Xiong, Q. Hu, and R. G. Song, *Appl. Surf. Sci.* 357, 1463 (**2015**).
2. R. Ambat, N. N. Aung, and W. Zhou, *Corros. Sci.* 42, 1433 (**2000**).
3. W. Zhou, T. Shen, and N. N. Aung, *Corros. Sci.* 52, 1035 (**2000**).
4. F. Cao, G. L. Song, and A. Atrens, *Corros. Sci*. 111, 835 (**2016**).
5. B. J. Lee, *J. Mater. Res.* 14, 1002 (**1999**).
6. M. X. Zhang, K. C. Hsieh, J. Dekock, and Y. A. Chang, *Scripta. Metall. Mater.* 27, 1361 (**1992**).
7. K. I. Jung, T. W. Kim, U. Paik, and K. S. Lee, *J. Korean. Ceram. Soc.* 43, 498 (**2006**).
8. H. M. A. El-Lateef and M. M. Khalaf, *Mater. Charact.* 108, 29 (**2015**).
9. M. W. Finnis, *J. Phys: Condens. Matter.* 8, 5811 (**1996**).
10. C. Li, R. Wu, A. J. Freeman, and C. L. Fu, *Phys. Rev. B* 48, 8317 (**1993**).
11. D. Liu, Y. Gao, J. Liu, K. Li, F. Liu Y. Wang, and L. An, *J. Eur. Ceram. Soc.* 36, 2051 (**2016**).
12. L. Wu, H. Zhu, X. Gai, and Y. Wang, *J. Prosthet. Dent.* 111, 51 (**2014**).
13. N. Xiang, X. Z. Xin, J. Chen, and B. Wei, *J. Dent.* 40, 453 (**2012**).
14. F. Hossein-Babaei, M. Gharesi, and M. Moalaghi, *ACS Appl. Mater. Inter.* 9, 26637 (**2017**).
15. L. Yuan, B. Ma, Y. Du, G. Li, Q. Zhu, and J. Yu, *J. Ceram. Process. Res.* 18, 352 (**2017**).
16. M. Trunec and K. Maca, *J. Am. Ceram. Soc.* 90, 2735 (**2007**).
17. J. H. Jang, I. H. Oh, J. W. Lim, and H. K. Park, *J. Ceram. Process. Res.* 18, 477 (**2017**).
18. H. Li, K. Liang, L. Mei, S. Gu, and S. Wang, *J. Matter. Sci. Lett.* 20, 1081 (**2001**).
19. J. P. Kruth, X. Wang, T. Laoui, and L. Froyen, *Assembly Autom.* 23, 357 (**2003**).
20. E. O. T. Olakanmi, R. F. Cochrane, and K. W. Dalgarno, *Prog. Mater. Sci.* 74, 401 (**2015**).
21. I. Shishkovsky, I. Yadroitsev, P. Bertrand, and I. Smurov, *Appl. Surf. Sci.* 254, 966 (**2007**).
22. P. Bertrand, F. Bayle, C. Combe, P. Gœuriot, and I. Smurov, *Appl. Surf. Sci.* 254, 989 (**2007**).
23. N. A. H. Husain, J. Camilleri, and M. Özcan, *J. Mech. Behav. Biomed.* 64, 104 (**2016**).
24. M. H. Bocanegra-Bernal, C. Dominguez-Rios, J. Echeberria, A. Reyes-Rojas, A. Garcia-Reyes, and A. Aguilar-Elguezabal, *Ceram. Int.* 42, 16417 (**2016**).
25. P. J. Kolmhofer, S. Eschlboeck-Fuchs, N. Huber, R. Rössler, J. Heitz, and J. D. Pedarnig, *Spectrochim. Acta B* 106, 67 (**2015**).

Received: 9 May 2018. Accepted: 26 June 2018.